Evaluating Damage with Digital Image Correlation: C. Applications to Composite Materials

39

François Hild, Jean-Noël Périé, and Stéphane Roux

Contents

Abstract

The present chapter is devoted to the evaluation of damage with digital image correlation (DIC). Applications will focus on composite materials. The latter ones are designed to accommodate microcracks through suited microstructures. As such, they constitute a natural class of materials for which damage (or rather damages) is an essential feature of their mechanical behavior. As discussed in a previous chapter (addressing detection of physical damage), DIC can reveal the elementary mechanisms (e.g., dense distribution of microcracks, crack branching along weak interfaces, progressive debonding of interfaces, and subsequent pullout or delamination). It will also be shown that damage laws can be identified with the help of DIC from mechanical tests imaged at different stages of loading. The followed strategy will be seen as reminiscent of the one that was used in the previous chapter dedicated to 1D (i.e., beam like) geometries (from physical to mechanical damage). Here, it will be necessary to couple DIC

F. Hild (✉) • J.-N. Périé • S. Roux
LMT-Cachan, ENS Cachan/CNRS/PRES UniverSud Paris, Cachan Cedex, France
e-mail: hild@lmt.ens-cachan.fr; jean-noel.perie@iut-tlse3.fr; stephane.roux@lmt.ens-cachan.fr

© Springer Science+Business Media New York 2015

G. Z. Voyiadjis (ed.), *Handbook of Damage Mechanics*,
DOI 10.1007/978-1-4614-5589-9_26

with finite element models. The benefit will be that in addition to the identified law, a full validation is naturally offered from the highly redundant piece of information contained in the measured displacement fields.

Identification of Mechanical Damage

This chapter follows the same footsteps as illustrated in the previous chapter based on beam geometry, but here it is dedicated to two- and three-dimensional systems. In spite of the fact that the examples concern composite materials, the methods are not limited to this class of materials.

When trying to identify damage from a mechanical test, the first step deals with the measurement of displacement fields. One of the measurement techniques is DIC, even though others can be used (e.g., grid methods, holography, and speckle interferometry). The outputs are displacement and strain fields that need to be post-processed. The damage variable(s) is(are) still hidden within these data. Inversion and identification techniques need to be used to extract mechanical damage fields. The problem thus consists of the evaluation of the local elastic properties, expressed as a relative loss of stiffness, $D(\mathbf{x})$ (where D can be a scalar or a tensor). This is a second step in which different metrics can be used to measure the distance between experimental measurements and numerical simulations (Avril et al. 2008; Grédiac and Hild 2012). This is a first route for identifying damage fields.

It is to be emphasized that the extraction of $D(\mathbf{x})$ from necessarily noisy kinematic fields is a difficult inverse problem (Tikhonov and Arsenin 1977). One way to help this determination is to assume that the same damage growth law applies everywhere within an analyzed material or structure. Thus, the unknowns are no longer a damage field but the parameters of a growth law. This represents a very drastic reduction in the number of unknowns, and hence it opens the way to a large reduction in the uncertainty of local damage. The assumption of a homogeneous constitutive law can be (or has to be) questioned. The invaluable advantage of dealing with field measurements, namely, the considerable amount of information, can be exploited to validate all assumptions proposed along the analysis. The pixel-wise comparison of measured and identified displacement fields or even images (e.g., computing the residual $\rho(\mathbf{x})$ fields (see Eq. (A.1)) from these different displacements) brings to light either the quality of the solution or its deficiencies. From the latter, it is generally clear to draw directions of progress or sophistication of, say, the constitutive law to reach a more satisfactory agreement.

A more elaborate strategy consists of coupling the measurement and identification steps. The unknowns to be measured associated with the trial displacement are no longer the standard degrees of freedom (e.g., nodal displacements in a Galerkin approach to DIC) but the parameters of the damage growth law in addition to boundary conditions to make the problem well posed. This type of global approach is referred to as *integrated* since the measured displacement field

is also mechanically admissible and yields mechanical parameters. An example of such an approach dedicated to beams was shown in "▶ Chap. 38, Evaluating Damage with Digital Image Correlation: B. From Physical to Mechanical Dam age" (see also Hild et al. 2011). The chosen displacement basis is either a closed-form solution (e.g., in a Brazilian test to identify elastic parameters (Hild and Roux 2006) or stress intensity factors in elastic media (Roux and Hild 2006)). The results of a numerical simulation can also be used to define the kinematic basis (e.g., in elasticity (Leclerc et al. 2009; Réthoré et al. 2009) or when dealing with damage (Réthoré 2010)).

Types of Damage and Constitutive Laws

When studying composite materials, one underlying difficulty is that the various damage mechanisms are strongly related to the material architecture, namely, particulate composites (Fig. 12 of "▶ Chap. 37, Evaluating Damage with Digital Image Correlation A. Introductory Remarks and Detection of Physical Damage"), composites with short fibers, and composites with continuous fibers (e.g., layered (Fig. 1 of "▶ Chap. 37, Evaluating Damage with Digital Image Correlation A. Introductory Remarks and Detection of Physical Damage"), woven, woven + stitched, interlock configurations) do not experience the same type of degradations. One of the consequences is that there are numerous models to describe their behavior (Orifici et al. 2008). Furthermore, there are also different possible choices for the smallest scale of modeling (i.e., microscopic (Burr et al. 1997), mesoscopic (Ladevèze 1992), or macroscopic (Périé et al. 2009)) to determine the behavior at the macroscopic scale, which is usually needed to run numerical simulations.

One modeling issue is to use either a discrete or continuum description of damage (Hild 2002). This choice will have consequences on the way damage is modeled and therefore experimentally characterized and identified. For example, in section "▶ Cracking in a Layered Composite" of "▶ Chap. 37, Evaluating Damage with Digital Image Correlation A. Introductory Remarks and Detection of Physical Damage," a continuum point of view was used to analyze the DIC results at the macroscopic scale (Figs. 2 and 3 of that chapter) of a 3-layer carbon-epoxy composite. However, mesoscopic observations are also possible, in particular to analyze the damage mechanisms.

Figure 1 shows the longitudinal displacement field where the individual damage mechanisms can be clearly read. It corresponds to an incremental approach where the reference configuration is chosen for a stress level of 1,120 MPa and 1,190 MPa in the deformed configuration. It becomes even clearer when analyzing the longitudinal strain field in which the two transverse cracks are observed. The lower crack, which initiated between these two stress levels, is more open than the upper one that initiated at an earlier stage. When analyzing the shear strain field, it is concluded that transverse cracking is accompanied by mesodelamination along the 0/90° interface for the lower crack. For the upper crack, mesodelamination has not evolved significantly.

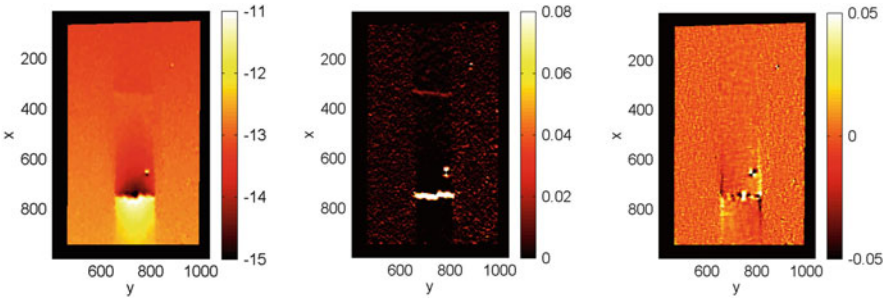

Fig. 1 (*Left*) Vertical displacement expressed in pixels (1 pixel $\leftrightarrow$ 3.5 µm), longitudinal strain (*center*), and in-plane shear strain (*right*) showing a transverse crack and mesodelamination. Note that another transverse crack ($x \approx 380$ pixels) that was created at a previous stage of loading is also visible. These results were obtained with regularized T3-DIC ($\ell = 5$ pixels, $\ell_m = 20$ pixels, $\ell_b = 10$ pixels). The region of interest has an area of $\approx 3 \times 2$ mm^2

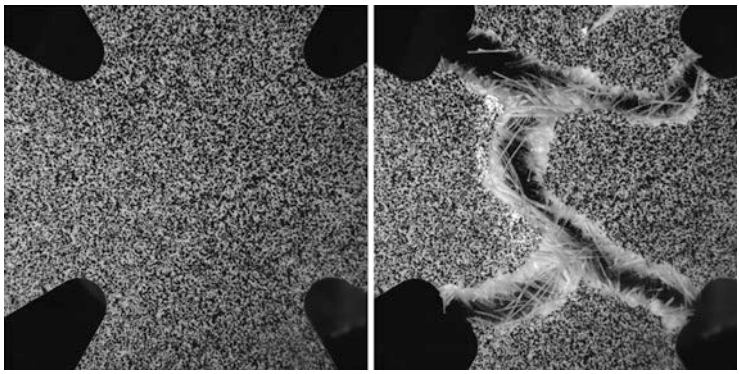

Fig. 2 Image of the sample prior to loading (*left*) and after failure (*right*). The observed region has an area of $\approx 68 \times 68$ mm^2

At this scale, an appropriate mechanical description would imply modeling the crack pattern in details, in particular, the combined effect of transverse cracking and mesodelamination, and the fact that the stresses in the vicinity of existing cracks are partially relaxed so that crack initiations are prevented very close to existing ones (this is a nonlocal effect). This hypothesis (Curtin 1991) allows the cracking pattern observed at the mesoscopic scale to be understood. It can be generalized to other situations dealing with multiple cracking (Hild 2002; Malésys et al. 2009; Forquin and Hild 2010; Guy et al. 2012).

When modeling the mechanical behavior of composite materials, the framework of continuum thermodynamics (Germain et al. 1983) turns out to be particularly powerful when applied to damage models. When cracks are described, it is more natural to express the state potential in terms of Gibbs' free enthalpy. However, in

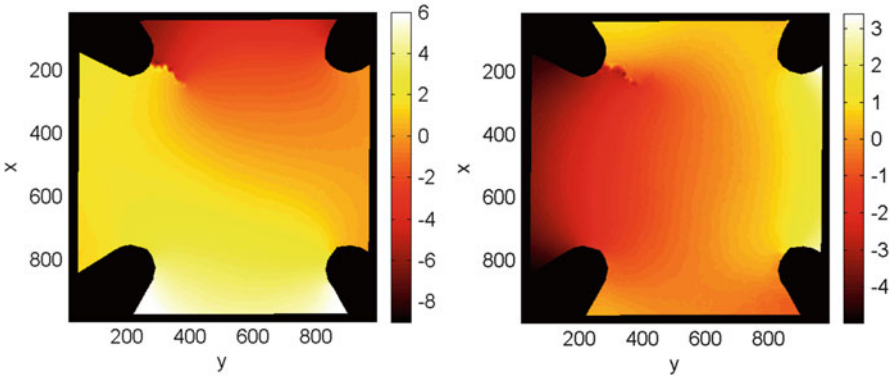

Fig. 3 Vertical (*left*) and horizontal (*right*) component of the displacement field (expressed in pixels) obtained from Q4-DIC ($\ell = 16$ pixels). The physical size of one pixel is 68 μm, and the region of interest has an area of $\approx 68 \times 68$ mm^2

numerical simulations, most of the formulations are displacement based, and it is therefore more convenient to consider Helmholtz' free energy density

$$\Psi = \frac{1}{2}\boldsymbol{\varepsilon}^e : \mathbf{C}(\mathbf{D}) : \boldsymbol{\varepsilon}^e + \Psi^{s-r}\left(\boldsymbol{\varepsilon}^i, \boldsymbol{\varepsilon}^c, \mathbf{d}, \mathbf{D}\right) \quad \text{with} \quad \boldsymbol{\varepsilon} = \boldsymbol{\varepsilon}^e + \boldsymbol{\varepsilon}^i + \boldsymbol{\varepsilon}^c \tag{1}$$

where $\boldsymbol{\varepsilon}$ is the infinitesimal strain tensor, $\boldsymbol{\varepsilon}^e$ the elastic strain tensor, $\boldsymbol{\varepsilon}^c$ the creep strain tensor (when needed (Begley et al. 1995; Du et al. 1997; Burr et al. 2001)), $\boldsymbol{\varepsilon}^i$ the inelastic strain tensor modeling all damage mechanisms leading to frictional sliding (e.g., fiber/matrix sliding, mesodelamination), $\mathbf{C}$ the macroscopic Hooke's tensor that contains various damage variables $\mathbf{D}$, and Ψ^{s-r} the stored and relaxed energy densities (Boudon-Cussac et al. 1998). In many models, inelasticity is described by resorting to isotropic hardening (e.g., Ladevèze and Le Dantec 1992). However, by using homogenization techniques, it is more natural to choose kinematic hardening (Andrieux et al. 1986; Hild et al. 1996) because it is associated with frictional sliding.

It can also be noted that when frictional sliding occurs, damage variables $\mathbf{d}$ are involved in the expression of the stored part of the state potential (Andrieux et al. 1986; Burr et al. 1997). Conversely, the relaxed part is caused by damage variables $\mathbf{D}$ that also lead to a stiffness loss (e.g., matrix-cracking in the presence of an initial residual stress field induced, say, by coefficient of thermal expansion mismatches (Budiansky et al. 1986; Boudon-Cussac et al. 1998) that is partially relaxed). Creep also involves a change in the self-balancing stress field, and therefore Ψ^{s-r} varies accordingly. Interfacial wear is a fatigue mechanism of many composite materials (Rouby and Reynaud 1993). It leads to a variation of the interfacial properties that influence the inelastic strain and the stored part of Ψ^{s-r} (Burr et al. 1998).

Furthermore, the state potential is generally postulated, and then the growth laws of the internal variables are written in terms of their associated forces obtained as partial derivatives of the state potential with respect to the former or combinations thereof. One critical issue to properly compute the dissipated energy is to evaluate

the part of the state potential Ψ^{s-r} that is stored or relaxed. The latter is the elastic energy density associated with the residual stresses induced by all dissipative mechanisms (Boudon-Cussac et al. 1998; Vivier et al. 2009, 2011).

Last, crack closure may occur, typically for mode I microcracks. This closure induces modeling issues that are not easy to tackle (Ladevèze et al. 1983; Chaboche et al. 1990; Desmorat 2000; Halm et al. 2002). Special care has to be exercised to avoid numerical and theoretical difficulties. This point will not be addressed herein. However, it can be noted that DIC (Hamam et al. 2007) and DVC (Limodin et al. 2009) can be used to analyze this phenomenon at different scales.

Damage in Low-Cost Composite

Two approaches are followed to study a vinylester matrix reinforced by an isotropic distribution of E-glass fibers. The first one consists of determining the contrast field of elastic stiffness, which can be interpreted as a signature of damage in a CDM context thanks to the coupling between elasticity and damage. The second one aims at identifying the growth law of an isotropic damage variable. Since only one internal (damage) variable is considered, any nonlinearity is attributed to damage. Consequently, the identification procedure does not need unloadings.

A thin plate made of this composite is prepared as a cross with wide arms, and subjected to biaxial loading (Fig. 2). The white surface of the test piece is sprayed with black paint so as to produce a fine random texture, which is needed for DIC. Digital images of the surface are shot for every 1-kN load increment in both directions up to complete failure, which occurred for 11.1 kN. Thus, 11 images are available for the analysis. The physical size of one pixel is 68 μm. In the sequel, this experiment is used to illustrate the results that are achieved when first seeking a stiffness field and second when identifying a damage law.

Inversion: Determination of Stiffness Field

In this first case, a field of elastic properties that account for the measured displacement field is sought. In the present case, Q4-DIC is considered (Fig. 3). The number of degrees of freedom in the inverse problem is of the same order of magnitude as the data (here the measured displacement field). The solution consists of the *inversion* of the mechanical problem.

It is assumed that the damage mechanism induces a heterogeneous contrast field such that the local Young's modulus is reduced to $\chi(\mathbf{x})E_0$ from its initial value E_0 while the Poisson's ratio, ν, remains unaltered. The equilibrium gap method (Claire et al. 2004) consists of exploiting the equilibrium equation

$$\mathrm{div}[\chi(\mathbf{x})\mathbf{C}_0\boldsymbol{\varepsilon}(\mathbf{u}(\mathbf{x}))] = \mathbf{0} \tag{2}$$

written here in the absence of body forces. The strain tensor $\boldsymbol{\varepsilon}$ is computed from the measured displacement field, and $\mathbf{C}_0$ is Hooke's tensor of the virgin material. Since

the displacement field is decomposed over a finite element basis (made of Q4 elements), the corresponding discretization of the "equilibrium gap" f_i is considered

$$f_i = \chi^m K_{ij}^m u_j = 0 \tag{3}$$

where K_{ij}^m is a component of the elementary rigidity matrix of the undamaged element m relating the displacement component u_j to the nodal force f_i^m (whose sum over all m elements should be equal to 0 for inner nodes). The rigidity matrix is linearly dependent upon the contrast χ. As can be seen from Eq. (3), since no static information is used (the right-hand side is vanishing at all inner nodes), the χ-field is determined up to an arbitrary scale factor. This is the consequence of limiting the analysis to the knowledge of kinematic data only. Only elastic *contrasts* can be determined in the present case. The formulation is complemented by arbitrarily prescribing that the average χ is equal to a constant. This is achieved by using a Lagrange multiplier or by eliminating one contrast value.

The inversion problem is ill-posed and some regularization is called for. The most straightforward approach is to search for the "best" solution for the χ-field in a subspace of smoothly varying fields in space. Q4 finite elements are used in the following, with however a mesh that is independent of (and coarser than) the measurement mesh. Shape functions N_i^m are introduced to provide the weight of the center of an element m for the i-th basis function

$$\chi^m = N_i^m b_i \tag{4}$$

where b_i are the unknown contrasts collected in a vector $\{\mathbf{b}\}$. This regularization limits the number of degrees of freedom $\{\mathbf{b}\}$, and hence the contrast field is obtained through the minimization of the global equilibrium gap

$$W(\{\mathbf{b}\}) = \sum_j \left(\sum_{i,m} L_j^m N_i^m b_i \right)^2 - \lambda \sum_{i,m} N_i^m b_i \tag{5}$$

where $L_j^m = K_{jk}^m u_k$ and λ is the Lagrange multiplier of the average contrast constraint. The minimization of functional W results in a linear problem that provides $\{\mathbf{b}\}$ amplitudes and, thus from Eq. (4), the contrast value in each element.

The final stage of loading is considered with a coarse mesh (10×10 elements) and a finer one (20×20 elements) for the contrast field (Fig. 4), which is to be compared with a 67×66 element mesh for the kinematic measurements (Fig. 3). In both cases, the stiffness reached a negative value at the top left corner (-0.02 and -0.3, respectively, for the coarse and fine meshes). This value has been artificially reset to 0.01. A satisfactory agreement between both results is obtained with a clear detection of crack initiation and propagation.

To evaluate the quality of the obtained contrast map, it is possible to resort to a standard elastic computation based on the determined stiffness contrast and using

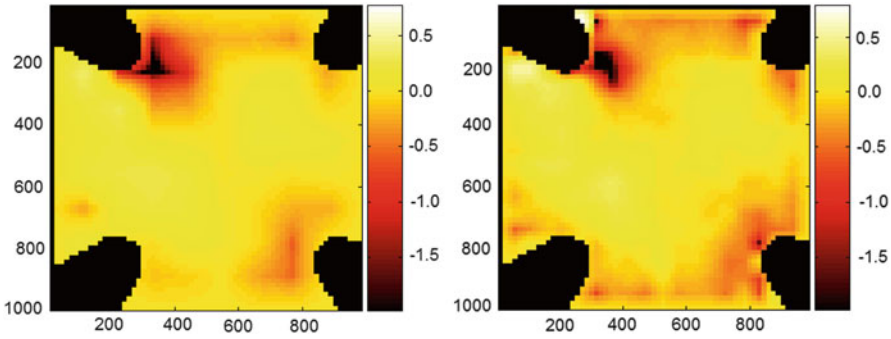

Fig. 4 Map of $\log_{10}\chi$ obtained for a coarse (10×10 elements, *left*) and fine (20×20 elements, *right*) mesh. The region of interest has an area of $\approx 68 \times 68$ mm^2

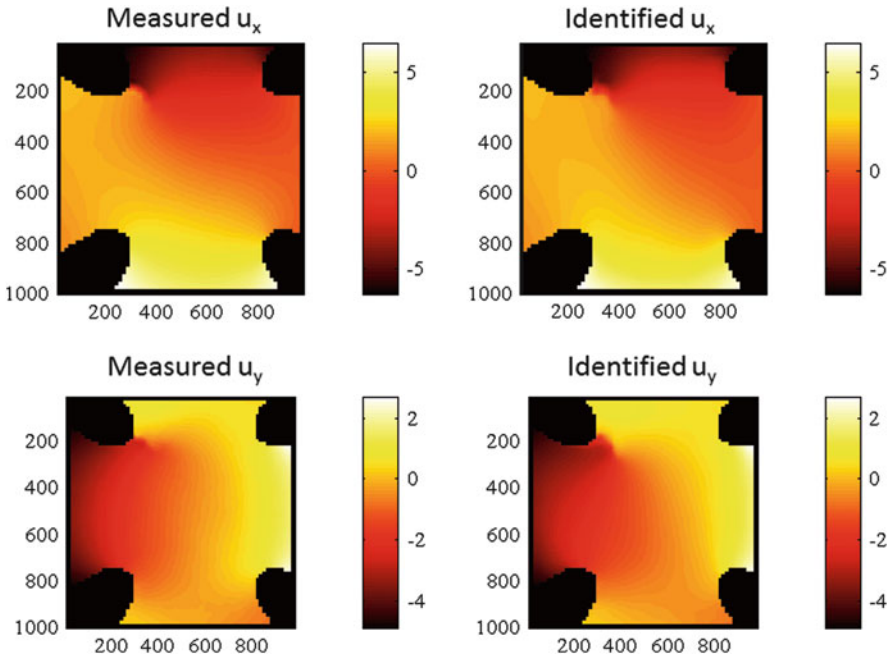

Fig. 5 Comparison between measured by Q4-DIC with $\ell = 16$ pixels (*left*) and recomputed (*right*) displacements expressed in pixels from the identified contrast field (fine mesh: 20×20 elements). The physical size of one pixel is 68 μm, and the region of interest has an area of $\approx 68 \times 68$ mm^2

Dirichlet boundary conditions, i.e., prescribing the displacement field on the boundary of the considered domain. The computed displacement field is then compared with the measured field in Fig. 5. A good agreement between both fields is observed.

To quantify the agreement, the following dimensionless "residual" ρ_u is defined: it is the standard deviation of the difference between identified and measured displacement

fields, normalized by the standard deviation of the measured displacement field. In the present case, for a fine mesh (i.e., 20×20 elements), this residual amounts to 14 %. The latter level is fair, and part of the discrepancy is related to the localized nature of damage, which cannot be fully captured with the chosen discretization.

Identification: Damage Growth Law

When a series of pictures is analyzed, there is no link between the contrast fields that can be determined by following the previous procedure. In particular, the choice of the additional condition to make the system invertible should be adapted to translate the contrast fields into damage fields. A growth law can be identified, but only by post-processing the previous results (Claire et al. 2007).

In the following, a regularized approach (Roux and Hild 2008) will be developed to move from an inversion to an identification (of a few material parameters). The spirit of the method is to require that elements with the same equivalent strain should also have the same damage level. This is a very strong requirement that allows the number of unknowns to be drastically reduced.

An isotropic description of damage is assumed to be valid. The behavior will be modeled by a unique scalar, $D(\mathbf{x})$, such that the Young's modulus is reduced to $(1-D)E_0$, from its initial value E_0, while the Poisson's ratio, ν, remains unaltered. The growth law of the damage variable D is described by a function of an equivalent strain ε_{eq} to be defined later on. The fact that D is related to ε_{eq} makes the identification easier since, if the damage parameter is assumed to be uniform over, say Q4 elements of the measurement mesh, it suffices to compute the equivalent strain per element before starting the identification procedure. The equilibrium gap norm is now written as

$$\mathfrak{R} = \sum_j \left(\sum_e L_j^e (1 - D^e) \right)^2 \tag{6}$$

and a decomposition of the damage growth law is chosen

$$D = \sum_i c_i \varphi_i\left(\widetilde{\varepsilon}_{\text{eq}}\right) \quad \text{with} \quad \widetilde{\varepsilon}_{\text{eq}}(t) = \max_{0 \le \tau \le t} \varepsilon_{\text{eq}}(\tau) \tag{7}$$

where φ_i are chosen functions (e.g., based on exponentials (Burr et al. 1997; Baptiste 2002)) and c_i the unknown parameters to identify (their number remains limited to a few units). The minimization of the equilibrium gap leads to the following linear system

$$\sum_p \sum_{e,f} \left(\sum_j L_j^e L_j^f \right) \varphi_p\left(\widetilde{\varepsilon}_{\text{eq}}\right) \varphi_q\left(\widetilde{\varepsilon}_{\text{eq}}\right) c_p = \sum_{e,f} \left(\sum_j L_j^e L_j^f \right) \varphi_q\left(\widetilde{\varepsilon}_{\text{eq}}\right) \tag{8}$$

The additional requirement prescribed to set the contrast scale can be dropped if the condition $\varphi_i(0) = 0$ is satisfied. It is worth noting that even though the initial problem is strongly nonlinear, the final formulation leads to a linear system.

As introduced above, the operator $\mathbf{L}$ is linear in terms of the measured displacements and involves the (uniform) elastic properties of the virgin material. The sum $\sum_e L_j^e = f_j$ can be interpreted as a nodal resultant force. The elastic problem with prescribed Dirichlet boundary conditions and known body forces is well posed and can be inverted to evaluate the nodal displacements

$$u_i = S_{ij} f_j \tag{9}$$

with $[\mathbf{S}] = [\mathbf{K}_0]^{-1}$, where $[\mathbf{K}_0]$ is the stiffness matrix of the virgin material. By noting that $\mathbf{L}$ is a second-order differential operator, the following form

$$\widetilde{\mathfrak{R}}(c_k) = \left\| \sum_j S_{ij} \sum_e L_j^e \left[1 - \sum_k c_k \varphi_k\left(\widetilde{\varepsilon}_{eq}\right) \right] \right\|^2 \tag{10}$$

allows the identification problem to be better conditioned when compared to Eq. (6). By noting that $[\mathbf{S}][\mathbf{L}] = \{\mathbf{u}^{\text{meas}}\}$, the reconditioned equilibrium gap becomes a distance written in terms of displacements and not its second-order derivatives

$$\widetilde{\mathfrak{R}}(c_k) = \left\| u_i^{meas} - \sum_j S_{ij} \sum_e L_j^e \sum_k c_k \varphi_k\left(\widetilde{\varepsilon}_{eq}\right) \right\|^2 \tag{11}$$

so that the identification will be less sensitive to measurement uncertainties.

The damage model tuned hereafter uses Helmholtz' free energy density Ψ when elasticity is coupled with damage ($\varepsilon = \varepsilon^e$ and $\Psi^{s-r} = 0$), which is expressed as (Marigo 1981)

$$\Psi = \frac{1}{2} \boldsymbol{\varepsilon} : \mathbf{C}_0 (1 - D) : \boldsymbol{\varepsilon} \tag{12}$$

so that the thermodynamic force Y associated with the damage variable D reads

$$Y = -\frac{\partial \Psi}{\partial D} = \frac{1}{2} \boldsymbol{\varepsilon} : \mathbf{C}_0 : \boldsymbol{\varepsilon} \tag{13}$$

Consequently, the equivalent strain ε_{eq} becomes, under a plane stress hypothesis,

$$\varepsilon_{\text{eq}}^2 = \frac{Y}{E_0} = \frac{\langle \varepsilon_1 \rangle^2 + 2\nu \langle \varepsilon_1 \rangle \langle \varepsilon_2 \rangle + \langle \varepsilon_2 \rangle^2}{2(1 - \nu^2)} \tag{14}$$

where ε_1, ε_2 are the two in-plane eigen strains and ν Poisson's ratio of the undamaged material. The functions φ defining the damage growth law (Eq. (7)) are assumed to be described by exponentials

$$\varphi_i\left(\widetilde{\varepsilon}_{\text{eq}}\right) = 1 - \exp\left(\frac{-\widetilde{\varepsilon}_{\text{eq}}}{\varepsilon_{ci}} \right) \tag{15}$$

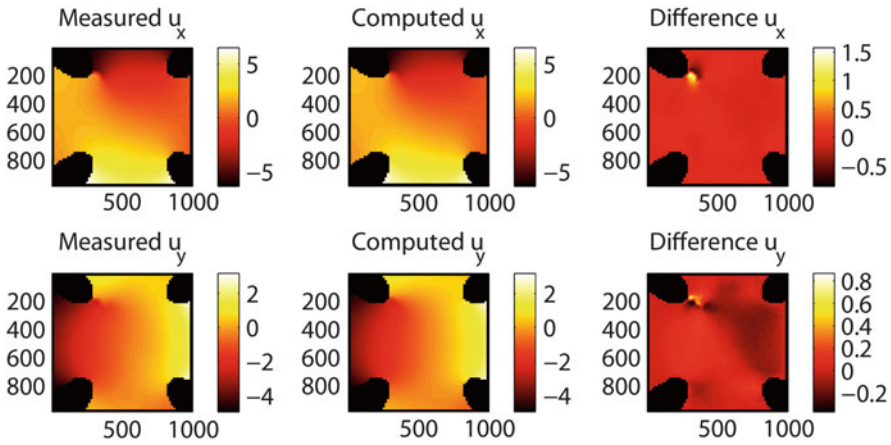

Fig. 6 Comparison between measured (*left*), identified (*center*) displacement fields at the final step of loading. The difference between the two displacements is also shown (*right*). The displacements are all expressed in pixels. The physical size of one pixel is 68 μm, and the region of interest has an area of $\approx 68 \times 68$ mm^2

where ε_{ci} are characteristic strains to be identified. Different characteristic strains in the damage law test functions were considered $\varepsilon_{ci} = 0.0067 \times (1, 2, 4, 8, 16)$ consistently with the range of equivalent strains encountered in the experiment. The five amplitudes were $\mathbf{c} = (0.87, 0, 0, 0, 0.13)$. The quality of the analysis appears to be good, namely, $\rho_u = 0.03, 0.03, 0.03$, and 0.05 for the last four load levels. It is worth noting that it is significantly lower than what was observed in the analysis of contrast fields.

Figure 6 shows a comparison between the measured and predicted displacement fields for the last load level. The fact that the quality deteriorates in this last level is due to a well-developed crack on the top left part of the sample. The crack is both crudely accounted for by the scalar damage model, but also presumably badly captured by the image correlation algorithm, which is designed for continuous displacement fields.

The damage map is very informative (Fig. 7a). Crack initiation on the left hand and top corner of the specimen is clearly captured, as also observed in the picture of step 11 (Fig. 2a) when magnified. Damage concentrations at other corners are also observed and correlate rather well with the final cracking pattern (Fig. 2b). The damage growth law consists of two regimes (Fig. 7b), possibly one prior to and one after damage localization. This problem will be addressed in section "Damage Localization Versus Cracking."

Anisotropic Damage Description for a Layered Composite

In the present section, the heterogeneity of the strain fields is enforced geometrically to ease the identification of the growth law. Consequently, the classical ±45° tensile test on coupons was modified by adding a lateral notch to the specimen.

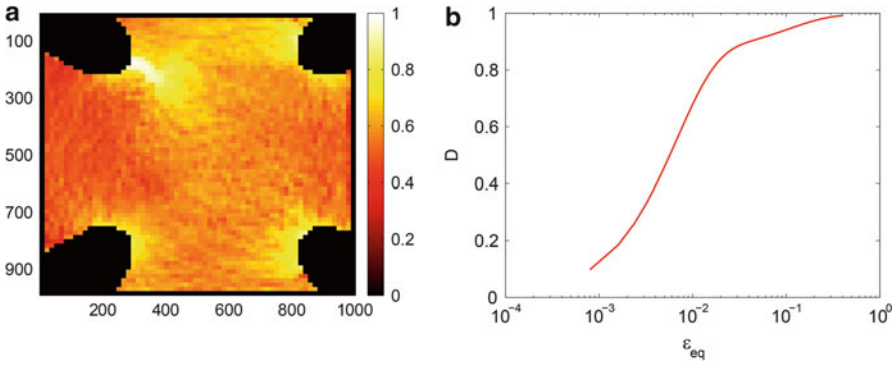

Fig. 7 (**a**) Maps of D for the last step of loading. One clearly sees in the left-hand top corner the initiation of a major crack that will lead to failure of the sample. Moreover secondary crack formations are also distinguished close to the other corners (see Fig. 2b for a detailed comparison with the final failure pattern). (**b**) Identified damage law

Each layer of the composite is made of unidirectionally aligned carbon fibers in a thermoset matrix. Contrary to the previous case, an anisotropic damage description is considered to describe the damage mechanism relative to shearing of the matrix. Gibbs' free enthalpy Φ of the composite then reads

$$\Phi = \frac{1}{2}\left[\frac{\sigma_{11}^2}{E_1} - \frac{\nu_{12}}{E_1}\sigma_{11}\sigma_{22} + \frac{\sigma_{22}^2}{E_2} + \frac{\sigma_{12}^2}{G_{12}(1-D)}\right] \tag{16}$$

where σ_{11}, σ_{22}, σ_{12} are the in-plane stress components expressed in the material frame (1, 2). The elastic properties are E_1 and E_2 (Young's moduli along the fiber directions), ν_{12} (Poisson's ratio), and G_{12} (in-plane shear modulus). The in-plane strain tensor $\boldsymbol{\varepsilon}$ is expressed as

$$\boldsymbol{\varepsilon} = \frac{\partial \Phi}{\partial \boldsymbol{\sigma}} \tag{17}$$

where $\boldsymbol{\sigma}$ is Cauchy's stress tensor and the thermodynamic force Y associated with the damage variable D becomes

$$Y = \frac{\partial \Phi}{\partial D} = \frac{\sigma_{12}^2}{2G_{12}(1-D)^2} = 2G_{12}\varepsilon_{12}^2 \tag{18}$$

Consequently, the equivalent strain becomes

$$\widetilde{\varepsilon}_{\text{eq}}(t) = \max_{0\le\tau\le t} |\varepsilon_{12}(\tau)| \tag{19}$$

The elementary stiffness matrix thus reads

$$[\mathbf{K}] = [\mathbf{K}_0] - D[\mathbf{K}_1] \tag{20}$$

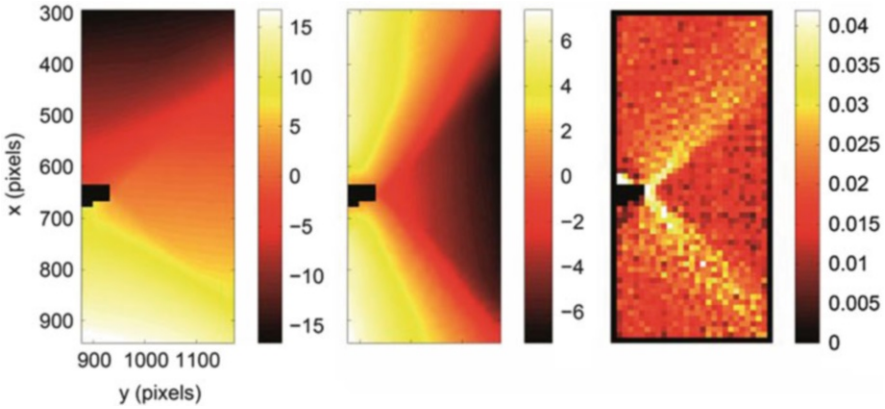

Fig. 8 Displacement maps u_x (*left*) and u_y (*center*) expressed in pixels (1 pixel $\leftrightarrow$ 36 µm) at maximum load (along the x-direction) of the notched specimen with a 12-pixel discretization. The rigid body motion was removed. Corresponding equivalent strain map ε_{eq} (*right*). Strain localization (along the fiber directions) is clearly visible. The region of interest has an area of $\approx 23.4 \times 10\ \text{mm}^2$

where $[\mathbf{K}_1]$ has only one nonzero (shear) term that is affected by damage. The reconditioned equilibrium gap becomes (Périé et al. 2009)

$$\breve{\mathfrak{R}}(c_k) = \left\| u_i^{meas} - \sum_j S_{ij} \sum_e \overline{L}_j^e \sum_k c_k \varphi_k\left(\widetilde{\varepsilon}_{eq}\right) \right\|^2 \tag{21}$$

with $\overline{L}_i^e = K_{ij}^{1e} u_j$.

In the following, 12-pixel Q4 element sizes are considered. The displacement maps are shown in Fig. 8 for the maximum load level (i.e., the last analyzed cycle). They are measured when the reference picture is the unloaded step after the maximum load level, which corresponds to the deformed configuration. The corresponding equivalent strain field is estimated by computing the average value in each finite element. The strain localization is clearly observed in the vicinity of the highly damaged (V-shaped) zones. Only the last of 14 loading/unloading cycles is shown herein. More results can be found in (Ben Azzouna et al. 2011).

By using the same expression as before for the damage law (15), the identification results yield the unknowns c_k for chosen characteristic strains ε_{ci}. The best solution is obtained when $\varepsilon_{ci} = 0.016 \times (1, 2, 4, 8)$ and $\mathbf{c} = (1.0, 0, 0, 0)$. The quality of the identification is first assessed globally by computing ρ_u. For the last load level, $\rho_u = 3.7$ %. This is a very low value giving confidence in the identification result. From the measurement of the equivalent strain map and the identified parameters of the damage law, it is possible to construct the damage maps for each analyzed cycle (Fig. 9 for the last five cycles).

For the last considered cycle (#14), a localized damage pattern is observed with a value of D approaching 1. This is in good accordance with the experimental failure

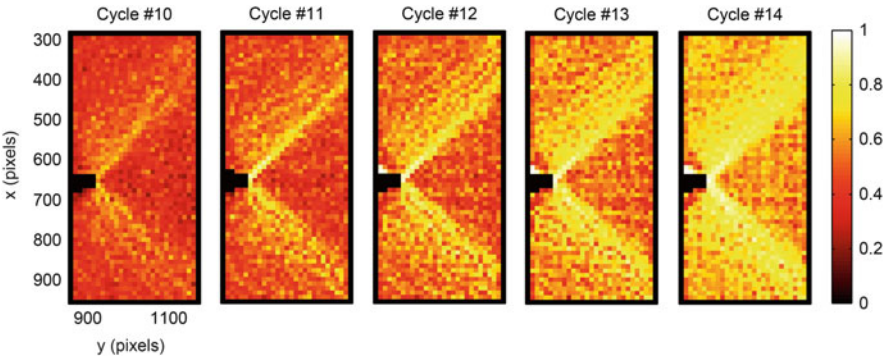

Fig. 9 Identified damage maps for the last five analyzed cycles

pattern (Ben Azzouna et al. 2011). The best solution is obtained with only one parameter ε_{c1} for which c_1 is therefore close to 1.

A first way of validating the identification results is to compare the computed displacement field using the damage law that was identified with the measured displacement field and then estimate the displacement residuals. Figure 10 shows the three maps corresponding to the displacement components for cycle #14. A very good agreement is observed.

Another way of validation is given by the damage law *itself*. The latter is compared with that obtained by following the classical identification procedure (Ladevèze and Le Dantec 1992). In the latter, only a single longitudinal strain level is available per unloading/loading cycle; from 10 to 15 points are generally accessible. For example, Fig. 11 shows the result from the analysis for which only five points lie above the damage threshold. With the present approach, the same results are shown in Fig. 11. Numerous identification points are available thanks to full-field data. It is also to be noted that the present approach allows for the identification of damage levels greater than 0.4, level at which the global method stops because of failure that occurs suddenly. In the range over which the two results can be compared, there is a good agreement, thereby validating the approach followed herein. It is to be remembered that the damage functions (15) do not incorporate a threshold parameter. This is the main difference between the two results. However, it is believed that this value is difficult to capture with fine meshes for which the measurement uncertainty is not sufficiently small.

Damage Localization Versus Cracking

The example of the cross-shaped composite sample discussed in section "Damage in Low-Cost Composite" is considered again. On the measurement side, a continuous displacement field was evaluated even at advanced stages of the experiment (Fig. 3). By analyzing the correlation residuals, it could have been concluded that the displacement continuity is questionable (Fig. 12), especially at the end of the experiment.

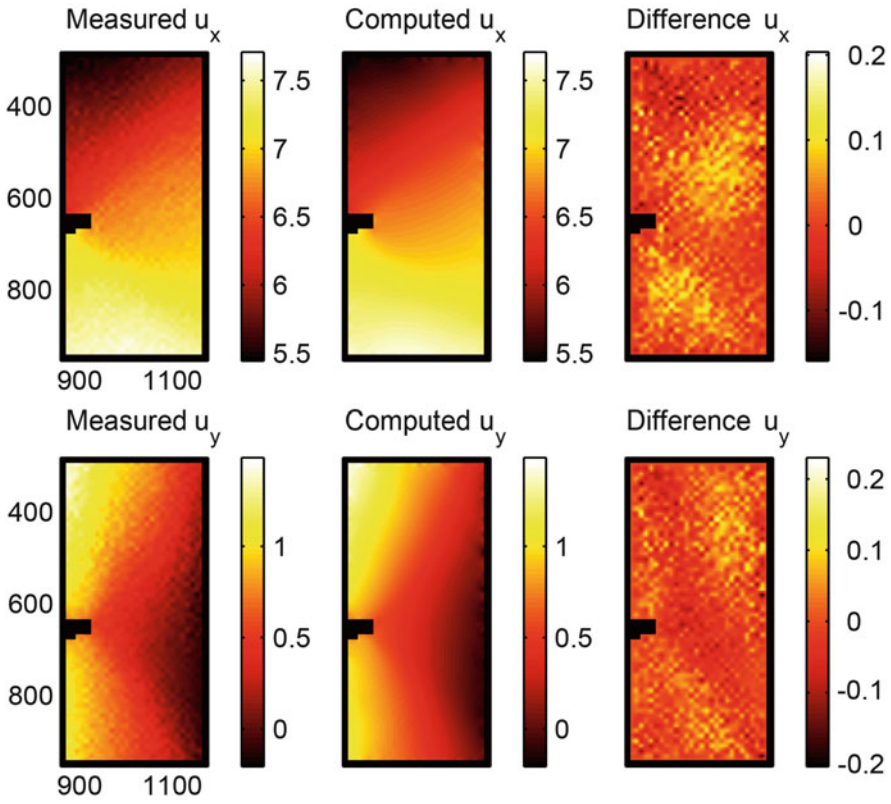

Fig. 10 Comparison of the measured and computed displacement fields for the last cycle (#14) for a 12-pixel discretization. The physical size of one pixel is 36 μm, and the region of interest has an area of $\approx 24.3 \times 10$ mm^2

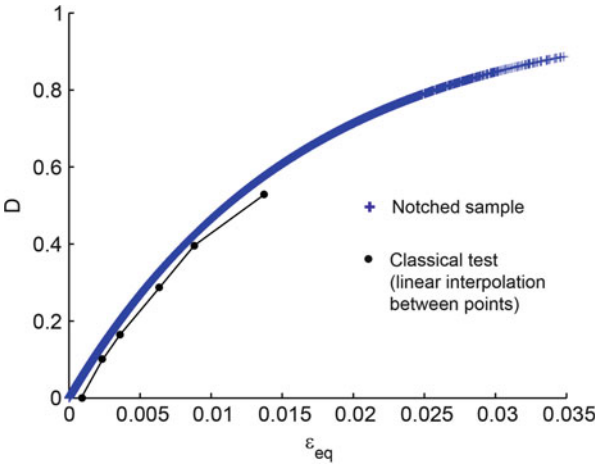

Fig. 11 Damage law identified by following the classical approach (few strain data are available) and by resorting to full-field measurements and the equilibrium gap method. Each cross corresponds to a measured strain

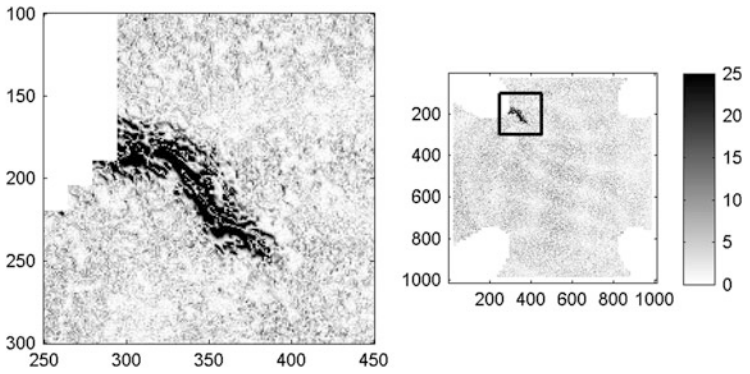

Fig. 12 Correlation residuals expressed in gray levels (the digitization of the analyzed pictures is 8 bits; see Fig. 2) for the displacement field shown in Fig. 3. The region of interest has an area of $\approx 68 \times 68$ mm^2. The crack is visible on the *top left corner* (see detail on the *left*)

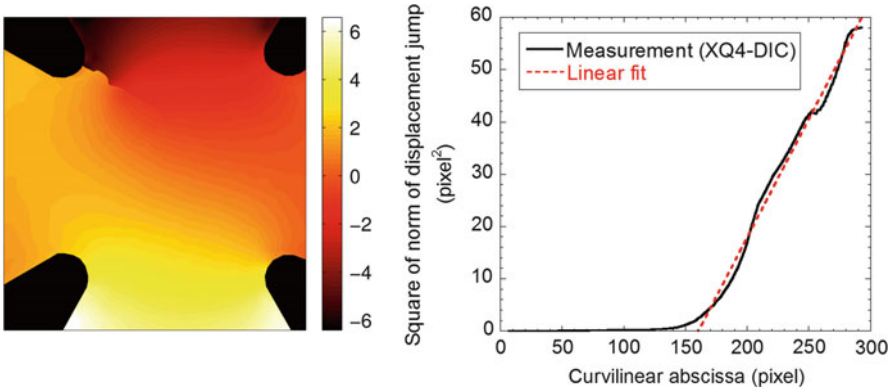

Fig. 13 Vertical (*left*) component of the displacement field (expressed in pixels) obtained from XQ4-DIC ($\ell = 32$ pixels). The region of interest has an area of $\approx 68 \times 68$ mm^2. Norm squared of displacement jump versus curvilinear abscissa (*right*). The physical size of one pixel is 68 μm (Courtesy of J. Réthoré)

To deal with displacement discontinuities in a global DIC context, two different routes can be followed. First, extended DIC (Réthoré et al. 2008) can be considered (e.g., XQ4-DIC). As in extended finite elements (Black and Belytschko 1999; Moës et al. 1999), it consists of enriching the displacement basis with discontinuous terms. Second, node splitting is also possible (Roux et al. 2012). Figure 13 shows the result obtained with XQ4-DIC. In particular, the crack opening displacement profile can be used to extract the stress intensity factor. In the plot of Fig. 13, the slope of the linear interpolation is equal to $8K/E_0\sqrt{2\pi}$, so that the value of the stress intensity factor K is 16 MPa $\sqrt{\text{m}}$.

On the modeling side, two regimes appear in the damage growth law shown in Fig. 7. The second one corresponds to strain levels that are greater than those

observed in tensile tests on the same material. They are related to the existence of a macrocrack whose description with CDM concepts may be questioned. To link linear elastic fracture mechanics and CDM, the dissipated energy (Lemaitre and Dufailly 1987) Δ is calculated by assuming a constant critical energy release rate G_c

$$\Delta = G_c a h \tag{22}$$

where a denotes the crack length and h the sample thickness. For the damage model, the dissipated energy density is first calculated for any broken element ($D = 1$)

$$\delta = \int_0^1 Y dD \tag{23}$$

With the chosen growth law, the dissipated energy density becomes

$$\delta = 2E_0 \sum_i c_i \varepsilon_{ci}^2 = 2Y_c \tag{24}$$

so that the dissipated energy of n broken elements reads

$$\Delta = n\ell^2 h\delta \tag{25}$$

where Y_c is the characteristic energy release rate density. By noting that $a \approx n\ell$, it follows

$$G_c = 2\ell Y_c \tag{26}$$

This result shows that the element size ℓ explicitly appears in the relationship between the critical energy release rate and the characteristic energy release rate density.

With the identified parameters of the damage growth law (see section "Identification: Damage Growth Law"), an estimate of the fracture toughness K_c is obtained

$$K_c = \sigma_c \sqrt{2\ell} \quad \text{with} \quad \varepsilon_c = \sqrt{\sum_i c_i \varepsilon_{ci}^2} \quad \text{and} \quad \sigma_c = E_0 \varepsilon_c \tag{27}$$

where σ_c denotes the characteristic strength and ε_c the characteristic strain. The fact that $\varepsilon_{c5} \gg \varepsilon_{c1}$ leads to the following approximation

$$K_c \approx E_0 \varepsilon_{c5} \sqrt{2\ell c_5} \tag{28}$$

This result proves that the second regime (i.e., for strain levels greater than 1 %) of the damage growth law (Fig. 7b) is associated with a localized mode (i.e., crack propagation) and not with a diffuse mechanism. The element size plays the role of a

nonlocal parameter. However, its physical meaning is lost since it was chosen at the measurement stage and not for any physical reason.

In the present case, it is found that $\sigma_c \approx 360$ MPa and $\varepsilon_c \approx 0.04$, with $\ell \approx 1.1$ mm and $E_0 = 9.3$ GPa. Consequently, the critical energy release rate becomes $G_c = 31$ kJ/m^2, and the corresponding fracture toughness $K_c = 17$ MPa$\sqrt{\text{m}}$. These values are rather high for composites. One of the reasons is due to the fact that a fiber mat allows cracks to be bridged, and therefore, brittle fracture is prevented from occurring. It was shown that this type of material is notch insensitive (Berthaud et al. 2000), which can be understood by the special architecture of the material. The level of fracture toughness is close to the value of the stress intensity factor estimated above. This constitutes a validation of the identification procedure.

Yet another way of modeling the presence of a crack and its process zone is to resort to cohesive zone models (CZMs). They consist of condensing all the nonlinearities along lines (in 2D simulations) and surfaces (in 3D simulations). However, contrary to standard fracture mechanics that only accounts for crack propagation (i.e., a crack is initially present in the considered structure), a CZM may account for initiation, propagation, and even coalescence when needed. One of the earlier models consists of writing the free energy density ψ of an elementary surface of the interface (Allix and Corigliano 1996) as

$$\psi = \frac{1}{2} k_n (1 - d) [u]^2 \tag{29}$$

where d denotes the interface damage variable, k_n the normal stiffness so that the normal traction t is related to the normal displacement jump $[u]$ by

$$t = \frac{\partial \psi}{\partial [u]} = k_n (1 - d) [u] \tag{30}$$

and the thermodynamic force y associated with the damage variable d reads

$$y = -\frac{\partial \psi}{\partial d} = \frac{1}{2} k_n [u]^2 \tag{31}$$

In the present case, only mode I is considered for the sake of simplicity. It can be generalized to account for the three fracture modes (Allix and Corigliano 1996).

When comparing Eqs. (12) and (13) with Eqs. (29), (30), and (31), the only difference is that the first ones are associated with energies per unit volume and the second ones by energies per unit surface. Consequently, if the free energies satisfy $\psi = \Psi \, \ell$, then the two damage variables are equal $d = D$ to achieve a total equivalence in terms of dissipated energy. It follows that the normal stiffness is such that $\ell \, k_n = E_0$, provided $\ell \, \varepsilon = [u]$, which is a good approximation in the present case.

Under these hypotheses, the parameters of the CZM are the normal stiffness $k_n = 4.3$ kN/mm^3, the characteristic strength $\sigma_c \approx 364$ MPa, and the characteristic crack opening displacement $\delta_c = \ell \, \varepsilon_c \approx 43$ μm (i.e., of the order of 0.6 pixel). In evaluating these parameters, the element size ℓ still appears.

It is of interest to draw an analogy with the lumped damage mechanics case that was discussed in "► Chap. 38, Evaluating Damage with Digital Image Correlation: B. From Physical to Mechanical Damage." The cantilever steel beam was shown to lead to a localized damage case. However, because the physical origin of this damage was a buckling of the beam walls, localization was distributed over a length scaling in proportion to the section. Yet, there is no obstacle to condense the nonlinear damage effect into a zone smaller than the actual one, provided the "damage" law is adjusted to the chosen size. To account for the same rotation, a curvature will have to scale as the inverse of the damaged zone. In the limit of a vanishing size, i.e., the "lumped" limit, the curvature diverges, but in such a way that the rotation undergoes a discontinuity. A quasi-perfect analogy exists with the crack versus localized damage discussion. Understanding what is a conventional choice and how physical quantities are to be scaled to comply with the chosen description shows the power of CDM and the sometimes heated debate around the notion of internal length scales, which used to be very active a few years back.

Conclusions and Perspectives

Among the various damage measurement methods discussed in the introduction (Part A), two of them were used. First, a detection technique was illustrated to analyze the development of physical microdamage (i.e., microcracks and microvoids) by resorting to 2D and 3D images, which are subsequently processed. Second, elasticity coupled with damage was utilized to invert damage fields and identify the parameters of a damage growth law. The choice of either approach is dictated by modeling strategies that mostly rely on the scale of observation and the taste of the scientist.

The identification of the (mechanical) damage law was first illustrated in the simple case of beam geometries (Part B) and then further applied herein to composite materials. The formulation of the damage law as one of the ingredients (together with equilibrium and compatibility) controlling the measured displacement field allows moving progressively to the analysis of a field of stiffness contrast and to robust determination of the damage growth law. Last, the question of the proper handling of a localized regime so that the chosen discretization remains compatible with the energy balance has been discussed both for lumped damage mechanics (for beams) and mesoscopic cracks (for composites). This very same path was followed both in the previous and present chapters.

To perform most of the analyses reported in this chapter, only one measurement technique (i.e., DIC) was used. Further, the identification procedures used the concept of equilibrium gap. It is worth noting that there are other full-field measurement and identification procedures (Grédiac and Hild 2012). The choice was made to link as strongly as possible both steps (i.e., measurement and identification). Global approaches to DIC are one way to achieve this goal and to seamlessly bridge the gap between experiments and numerical simulations.

In terms of damage models, only simple ones were used herein for illustration purposes and also because complexity has to be dealt with care. Inversion and identification belong to the class of inverse problems. Consequently, the more numerous the unknown parameters, the more measured data need to be collected to make the results trustworthy and robust. Further, only 2D displacement fields were used in this chapter. However, the identification procedures are generic and are currently being generalized to 3D surface and volume measurements.

As discussed in the introduction of Part A, various scales of measurement and modeling are possible when describing damage. For damage detection, different scales were considered. Smaller and larger ones can also be taken into consideration. For damage models, they were essentially written at the level of the volume element of continuum mechanics. Other choices could have been made.

All these developments are geared toward the emergence of simulation-based engineering sciences. Among the various challenges (Blue Ribbon Panel 2006), there are open problems associated with multiscale and multi-physics modeling. Continuum damage mechanics is one area of mechanics that needs further development to reach a level of confidence sufficiently high for engineers to use its models to design (damage-tolerant) structures. Real-time integration of simulation methods with measurement systems is another issue to be addressed. To achieve this goal, robust model identification and validation procedures need to be improved and made robust.

Acknowledgments Many results reported in this chapter have been obtained thanks to the help of and discussions with M. Ben Azzouna, S. Calloch, J.-M. Guimard, B. Leboime, J. Réthoré, and N. Swiergiel. Part of the work was supported by Agence Nationale de la Recherche (VULCOMP phases 1 and 2) and grants from Ile de France region (SESAME project entitled "*Plate-forme francilienne d' expérimentations mécaniques de 3^e génération*" and DICCIT project).

This chapter has been reviewed by Profs. A. Dragon and J. Lemaitre. The authors would like to warmly thank them for their patience and help in improving the compuscript. Last, this chapter is dedicated to Prof. F.A. Leckie (1929–2013) with whom the authors discussed many issues presented herein.

References

O. Allix, A. Corigliano, Modeling and simulation of crack propagation in mixed-modes interlaminar fracture specimens. Int. J. Fract. **77**, 111–140 (1996)

S. Andrieux, Y. Bamberger, J.-J. Marigo, Un modèle de matériau microfissuré pour les bétons et les roches. J. Méc. Th. Appl. **5**(3), 471–513 (1986)

S. Avril, M. Bonnet, A.-S. Bretelle, M. Grédiac, F. Hild, P. Ienny, F. Latourte, D. Lemosse, S. Pagano, E. Pagnacco, F. Pierron, Overview of identification methods of mechanical parameters based on full-field measurements. Exp. Mech. **48**(4), 381–402 (2008)

D. Baptiste, Damage micromechanics modelling of discontinuous reinforced composites, in *Continuum Damage Mechanics of Materials and Structures*, ed. by O. Allix, F. Hild (Elsevier, Amsterdam, 2002), pp. 115–163

M.R. Begley, A.G. Evans, R.M. McMeeking, Creep rupture in ceramic matrix composites with creeping fibers. J. Mech. Phys. Solids **43**(5), 727–740 (1995)

M. Ben Azzouna, J.-N. Périé, J.-M. Guimard, F. Hild, S. Roux, On the identification and validation of an anisotropic damage model by using full-field measurements. Int. J. Damage Mech. **20**(8), 1130–1150 (2011)

Y. Berthaud, S. Calloch, F. Collin, F. Hild, Y. Ricotti, Analysis of the degradation mechanisms in composite materials through a correlation technique in white light, in *Proceeding of the IUTAM Symposium on Advanced Optical Methods and Applications in Solid Mechanics,* ed. by A. Lagarde,(Kluwer, Dordrecht, 2000), pp. 627–634

T. Black, T. Belytschko, Elastic crack growth in finite elements with minimal remeshing. Int. J. Num. Meth. Eng. **45**, 601–620 (1999)

Blue Ribbon Panel, Simulation-Based Engineering Sciences. Final report, NFS (2006), www.nsf.gov/pubs/reports/sbes_final_report.pdf

D. Boudon-Cussac, A. Burr, F. Hild, On a continuum description of damage in fiber-reinforced composites, in *Proceedings of the McNU'97, Damage Mechanics in Engineering Materials,* eds. by G.Z. Voyadjis, J.-W.W. Ju, J.-L.Chaboche. Studies in applied mechanics, vol. 46 (Elsevier, Amsterdam, 1998), pp. 303–320

B. Budiansky, J.W. Hutchinson, A.G. Evans, Matrix fracture in fiber-reinforced ceramics. J. Mech. Phys. Solids **34**(2), 167–189 (1986)

A. Burr, F. Hild, F.A. Leckie, Continuum description of damage in ceramic-matrix composites. Eur. J. Mech. A/Solids **16**(1), 53–78 (1997)

A. Burr, F. Hild, F.A. Leckie, The mechanical behaviour under cyclic loading of ceramic-matrix composites. Mater. Sci. Eng. **A250**(2), 256–263 (1998)

A. Burr, F. Hild, F.A. Leckie, Isochronous analysis of ceramic-matrix composites under thermomechanical cyclic loading conditions. Comp. Sci. Tech. **61**(15), 2231–2238 (2001)

J.-L. Chaboche, On the description of damage induced anisotropy and active passive effect, in *Proceedings of the ASME Winter Annual Meeting,* 1990

D. Claire, F. Hild, S. Roux, A finite element formulation to identify damage fields: the equilibrium gap method. Int. J. Num. Meth. Eng. **61**(2), 189–208 (2004)

D. Claire, F. Hild, S. Roux, Identification of a damage law by using full-field displacement measurements. Int. J. Damage Mech. **16**(2), 179–197 (2007)

W.A. Curtin, Exact theory of fiber fragmentation in single-filament composite. J. Mater. Sci. **26**, 5239–5253 (1991)

R. Desmorat, Quasi-unilateral conditions in anisotropic elasticity. C. R. Acad. Sci. Paris IIB **328** (6), 445–450 (2000)

Z.Z. Du, A.C.F. Cocks, R.M. McMeeking, Power-law matrix creep in fiber composites due to transverse stress gradient. Eur. J. Mech. A/Solids **16**(3), 445 (1997)

P. Forquin, F. Hild, A probabilistic damage model of the dynamic fragmentation process in brittle materials. Adv. Appl. Mech. **44**, 1–72 (2010)

P. Germain, Q.S. Nguyen, P. Suquet, Continuum thermodynamics. ASME J. Appl. Mech. **50**, 1010–1020 (1983)

M. Grédiac, F. Hild (eds.), *Full-Field Measurements and Identification in Solid Mechanics* (ISTE/Wiley, London, 2012)

N. Guy, D.M. Seyedi, F. Hild, A probabilistic nonlocal model for crack initiation and propagation in heterogeneous brittle materials. Int. J. Num. Meth. Eng. **90**(8), 1053–1072 (2012)

D. Halm, A. Dragon, Y. Charles, A modular damage model for quasi-brittle solids – interaction between initial and induced anisotropy. Arch. Appl. Mech. **72**, 498–510 (2002)

R. Hamam, F. Hild, S. Roux, Stress intensity factor gauging by digital image correlation: application in cyclic fatigue. Strain **43**, 181–192 (2007)

F. Hild, Discrete versus continuum damage mechanics: a probabilistic perspective, in *Continuum Damage Mechanics of Materials and Structures*, ed. by O. Allix, F. Hild (Elsevier, Amsterdam, 2002), pp. 79–114

F. Hild, A. Burr, F.A. Leckie, Matrix cracking and debonding in ceramic-matrix composites. Int. J. Solids Struct. **33**(8), 1209–1220 (1996)

F. Hild, S. Roux, Digital image correlation: from measurement to identification of elastic properties – a review. Strain **42**, 69–80 (2006)
F. Hild, S. Roux, N. Guerrero, M.E. Marante, J. Florez-Lopez, Calibration of constitutive models of steel beams subject to local buckling by using digital image correlation. Eur. J. Mech. A/Solids **30**, 1–10 (2011)
P. Ladevèze, Sur une théorie de l'endommagement anisotrope. Internal report no. 34, LMT Cachan, 1983
P. Ladevèze, A damage computational method for composite structures. Comput. Struct. **44**(1–2), 79–87 (1992)
P. Ladevèze, E. Le Dantec, Damage modelling of the elementary ply for laminated composites. Comp. Sci. Tech. **43**(3), 257–267 (1992)
H. Leclerc, J.-N. Périé, S. Roux, F. Hild, Integrated digital image correlation for the identification of mechanical properties, in *Mirage*, ed. by A. Gagalowicz, W. Philips. LNCS, vol. 5496 (Springer, Berlin, 2009), pp. 161–171
J. Lemaitre, J. Dufailly, Damage measurements. Eng. Fract. Mech. **28**(5–6), 643–661 (1987)
N. Limodin, J. Réthoré, J.-Y. Buffière, A. Gravouil, F. Hild, S. Roux, Crack closure and stress intensity factor measurements in nodular graphite cast iron using 3D correlation of laboratory X ray microtomography images. Acta Mat. **57**(14), 4090–4101 (2009)
N. Malésys, L. Vincent, F. Hild, A probabilistic model to predict the formation and propagation of crack networks in thermal fatigue. Int. J. Fat. **31**(3), 565–574 (2009)
J.-J. Marigo, Formulation d'une loi d'endommagement d'un matériau élastique. C. R. Acad. Sci. Paris (série II) **292**, 1309–1312 (1981)
N. Moës, J. Dolbow, T. Belytschko, A finite element method for crack growth without remeshing. Int. J. Num. Meth. Eng. **46**(1), 133–150 (1999)
A.C. Orifici, I. Herszberg, R.S. Thomson, Review of methodologies for composite material modelling incorporating failure. Comp. Struct. **86**(1–3), 194–210 (2008)
J.N. Périé, H. Leclerc, S. Roux, F. Hild, Digital image correlation and biaxial test on composite material for anisotropic damage law identification. Int. J. Solids Struct. **46**, 2388–2396 (2009)
J. Réthoré, A fully integrated noise robust strategy for the identification of constitutive laws from digital images. Int. J. Num. Meth. Eng. **84**(6), 631–660 (2010)
J. Réthoré, F. Hild, S. Roux, Extended digital image correlation with crack shape optimization. Int. J. Num. Meth. Eng. **73**(2), 248–272 (2008)
J. Réthoré, S. Roux, F. Hild, An extended and integrated digital image correlation technique applied to the analysis fractured samples. Eur. J. Comput. Mech. **18**, 285–306 (2009)
D. Rouby, P. Reynaud, Fatigue behaviour related to interface modification during load cycling in ceramic-matrix fibre composites. Comp. Sci. Tech. **48**, 109–118 (1993)
S. Roux, F. Hild, Stress intensity factor measurements from digital image correlation: post-processing and integrated approaches. Int. J. Fract. **140**(1–4), 141–157 (2006)
S. Roux, F. Hild, Digital image mechanical identification (DIMI). Exp. Mech. **48**(4), 495–508 (2008)
S. Roux, F. Hild, H. Leclerc, Mechanical assistance to DIC, in *Proceedings of the Full Field Measurements and Identification in Solid Mechanics,* eds. by H. Espinosa, F. Hild. IUTAM Procedia, vol. 4 (Elesevier, 2012), pp. 159–168
A.N. Tikhonov, V.Y. Arsenin, *Solutions of Ill-Posed Problems* (Wiley, New York, 1977)
G. Vivier, H. Trumel, F. Hild, On the stored and dissipated energies in heterogeneous rate-independent systems: theory and simple examples. Continuum Mech. Thermodyn. **20**(7), 411–427 (2009)
G. Vivier, H. Trumel, F. Hild, On the stored and dissipated energies in heterogeneous rate-independent materials. Application to a quasi-brittle energetic material under tensile loading. Continuum Mech. Thermodyn **23**, 387–407 (2011)